ARTICLES

Micro-engineered local field control for high-sensitivity multispectral MRI

Gary Zabow[1,2], Stephen Dodd[1], John Moreland[2] & Alan Koretsky[1]

In recent years, biotechnology and biomedical research have benefited from the introduction of a variety of specialized nanoparticles whose well-defined, optically distinguishable signatures enable simultaneous tracking of numerous biological indicators. Unfortunately, equivalent multiplexing capabilities are largely absent in the field of magnetic resonance imaging (MRI). Comparable magnetic-resonance labels have generally been limited to relatively simple chemically synthesized superparamagnetic microparticles that are, to a large extent, indistinguishable from one another. Here we show how it is instead possible to use a top-down microfabrication approach to effectively encode distinguishable spectral signatures into the geometry of magnetic microstructures. Although based on different physical principles from those of optically probed nanoparticles, these geometrically defined magnetic microstructures permit a multiplexing functionality in the magnetic resonance radio-frequency spectrum that is in many ways analogous to that permitted by quantum dots in the optical spectrum. Additionally, *in situ* modification of particle geometries may facilitate radio-frequency probing of various local physiological variables.

Magnetic resonance imaging[1,2] has become a widely used medical diagnostic and research tool[3]. A key to this success has been the development of numerous chemically synthesized image-enhancing agents[4–8]. Nevertheless, MRI still lacks the sensitivity and the multiplexing capabilities of optical imaging, which can use coloured fluorophores[9], multi-spectral semiconductor quantum dots[10–12], metallic nanoparticles[13,14], and even microfabricated barcodes[15] for multifunctional encoding and biomolecular or cellular labelling, sensing and tracking. Because optically based labels can probe only so far beneath most surfaces, however, being able to distinguish with MRI between different types of cells, at the single-cell level, would be useful for cellular biology and early disease detection and diagnosis. Currently, however, MRI cell tracking is based on the magnetically dephased signal from the water surrounding cells labelled with many superparamagnetic iron oxide (SPIO) nanoparticles[6,16,17] or dendrimers[18], or individual micrometre-sized particles of iron oxide[19–21] (MPIOs). The continuous spatial decay of the external fields surrounding these, or any other, magnetizable particles imposes a continuous range of Larmor frequencies that broadens the water hydrogen proton line, obscuring distinction between different types of magnetic particles that might specifically label different types of cells. The utility of magnetic particles would be greatly enhanced if they could instead frequency-shift the water by discrete, controllable amounts, transforming an effectively monochrome contrast agent into a 'coloured' spectral set of distinguishable tags.

Here we consider the advantages of top-down microfabrication as an alternative to traditional bottom-up chemical synthesis for designing MRI contrast agents with more directly engineered properties and, accordingly, increased functionality. In particular, we demonstrate a new contrast agent imaging modality based on geometrical rather than chemical structure, showing how engineered magnetic microstructures can form effectively subcellular-sized radio-frequency identification (RFID) tags for multi-spectral MRI. Designed to exploit water diffusion, these microstructures locally increase MRI sensitivity by several orders of magnitude, yielding low concentration requirements and potentially enabling individually detectable, spectrally distinct micro-tags. With frequencies determined by structural shape and composition instead of by chemical[7] or nuclear[8] shift, spectral signatures can be tailored over very broad frequency shift ranges spanning many tens of thousands of parts per million. Beyond their radio-frequency analogy to continuously tunable optical quantum dots, such microstructures may also enable a variety of localized physiological probes, enhancing both MRI capabilities and basic biological research.

The potential of spectral shifting is indicated by recent interest in PARACEST[7] molecular complexes, whose chemical shifts can generate off-resonance MRI contrast through proton exchange. Unfortunately, relying on a restricted set of macromolecular structures, they have relatively limited shift ranges which may restrict their effectiveness and often necessitate high MRI fields. Here it is shown that instead of being constrained by any inherent chemical environment, it is possible to customize spectral shifts by microfabricating suitably shaped magnetizable elements. This increased design control allows shift ranges and sensitivities that far exceed those of existing molecular analogues, and enables a new class of MRI agent: single-particle spectral tags, which combine the advantages of single-particle tracking and distinct spectral shifting, while retaining compatibility with standard MRI hardware.

Magnetic structure design and operation

Spectral shifting by magnetic structures is made possible by noting that even though all magnetic objects have continuously decaying external fields, this does not preclude discretely frequency shifting MRI-detectable nuclei contained internally, either within a magnetizable shell or between neighbouring magnetizable elements. A distinct, resolvable frequency-shifted peak requires a spatially extended volume over which the additional field generated by the magnetizable structure is homogeneous and preferably offset in magnitude from that of the structure's surrounding external decaying fields. More precisely, because typical background MRI field magnitudes generally

[1]Laboratory of Functional and Molecular Imaging, National Institute of Neurological Disorders and Stroke, National Institutes of Health, Bethesda, Maryland 20892, USA.
[2]Electromagnetics Division, National Institute of Standards and Technology, Boulder, Colorado 80305, USA.

substantially exceed those of the magnetizable structures (at least in the regions of interest), quadrature addition implies that only that component of the structure's field parallel to the background field need strictly satisfy this homogeneity condition. Among several possible configurations that may be useful, we demonstrate here a spaced, magnetizable double-disk geometry that is illustrated schematically in Fig. 1, together with typical resulting magnetic field profiles. This particular geometry is attractive because, in addition to generating a highly homogeneous field over a large volume fraction, the particularly open nature of the design helps maximize water self-diffusion through the structure, enabling use of MRI techniques that can increase the signal-to-noise ratio over that of any closed structure.

The double-disk geometry is also inherently scalable and suited to parallel wafer-level microfabrication. Figure 2a–d shows scanning electron microscope (SEM) images of sample microfabricated structures. Full fabrication details are lengthy (G.Z., manuscript in preparation); briefly, particle complexes are surface micromachined through a combination of metal evaporation and electroplating depositions followed by lithographically defined ion-milling and selective wet etching. The disks are separated by non-magnetic spacers: either an internal metal post that remains after a timed etch, or external biocompatible[22,23] photo-epoxy posts. A final gold sputter-coating further enhances biocompatibility and access to thiol-based chemistry for specific surface functionalization if desired.

Although the structure's exact resonance frequency shift, $\Delta\omega$, depends on the fields generated throughout the volume between the disks, $\Delta\omega$ can be roughly approximated analytically from the field at the centre of the structure. For gyromagnetic ratio γ, and magnetically saturated disks of thickness h, radius R, centre-to-centre separation $2S$, and saturation magnetic polarization J_S, elementary magnetostatics gives $\Delta\omega = (\gamma J_S/2)[(S - h/2)/((S - h/2)^2 + R^2)^{1/2} - (S + h/2)/((S + h/2)^2 + R^2)^{1/2}]$. For thin disks with $h \ll 2S \approx R$, this reduces to:

$$\Delta\omega \approx -\gamma J_S \left(\frac{hR^2}{2(R^2 + S^2)^{3/2}} \right)$$

Spectral signatures can be tailored by modifying any of J_S, h, R, or S. All particles shown in this Article were made from nickel ($J_S \approx 0.5$–0.6 T), but could equally well be formed from other magnetic alloys. J_S can therefore be chosen anywhere from zero up to 2 T (soft iron), enabling large water shift ranges from 0 to of order of -10 MHz. Unlike frequency shifting based on chemical molecules, the frequency dependence on a dimensionless geometrical aspect ratio implies shifting of any nuclear species and by any overall particle size. For example, we demonstrate here frequency shifting of both hydrogen (Figs 3 and 4b–e) and deuterium (Fig. 4a) nuclei, and with particle size scales spanning three orders of magnitude, from millimetre to micrometre.

This frequency-shifting ability implicitly assumes alignment of the disk planes with the applied magnetizing MRI field, B_0. Such alignment is ensured by the structure's built-in magnetic shape anisotropy. Figure 2e demonstrates this, showing particles readily self-aligning even in small fields. Although aligning torques generally increase with increasing field, once typical MRI fields are reached, the structures' magnetic materials are already fully saturated and their Zeeman magnetostatic energies are therefore independent of particle orientation. In this regime, aligning torque magnitudes decouple from B_0 and are instead determined by the angular dependence of the magnetostatic demagnetization energy[24,25] that is proportional to J_S^2/μ_0, for free-space magnetic permeability, $\mu_0 = 4\pi \times 10^{-7}$ H m^{-1}. Specifically, assuming $h \ll R$, for any misalignment angles θ between B_0 and the disk planes, resulting magnetic torques on the disks produce self-aligning pressures of order $(h/(R^2 + S^2)^{1/2})(J_S^2/\mu_0)\sin(2\theta)$. This equates to pressures of order 10^{-8} to 10^{-6} N μm^{-2}. By comparison, even within cellular cytoplasm, yield stresses are only in the range 10^{-13} to 10^{-9} N μm^{-2} (refs 26, 27).

Being externally similar to MPIOs with comparable dipolar far-field decays, the structures can be spatially imaged via the same dephasing common to MPIOs; but in addition they can be differentiated spectrally and distinguished from spurious signal voids that confound SPIO/MPIO imaging. Depending on particle size, many different particle spectra can be acquired simultaneously from a single free induction decay following a broadband $\pi/2$ excitation. Alternatively, chemical shift imaging can spatially and spectrally resolve the tags simultaneously. Figure 3 demonstrates this spectral differentiation between individual particles. Because the spectra come from internal, rather than surrounding, water, spatial localization also improves substantially.

Diffusion-driven signal enhancement

Direct spectral imaging, however, is fundamentally limited by the relatively small number of nuclei within the structure that contribute to the signal. Our open structures, however, also allow an efficient analogue to magnetization transfer imaging[28,29], with diffusional exchange between water inside and outside the particle replacing traditional chemical exchange between bound and free protons. Therefore, using a preparatory set of $\pi/2$ pulses at the particle's shifted resonance to saturate out signal from a subsequent on-resonance pulse, the continual diffusion of fresh spins through the open particle structure can multiply its apparent signal volume. Scanned over off-resonant frequencies, this yields the so-called z-spectra[30] shown in Fig. 4b–e that also demonstrate how resonances can be engineered by manipulating structure geometry. Alternatively, fixing

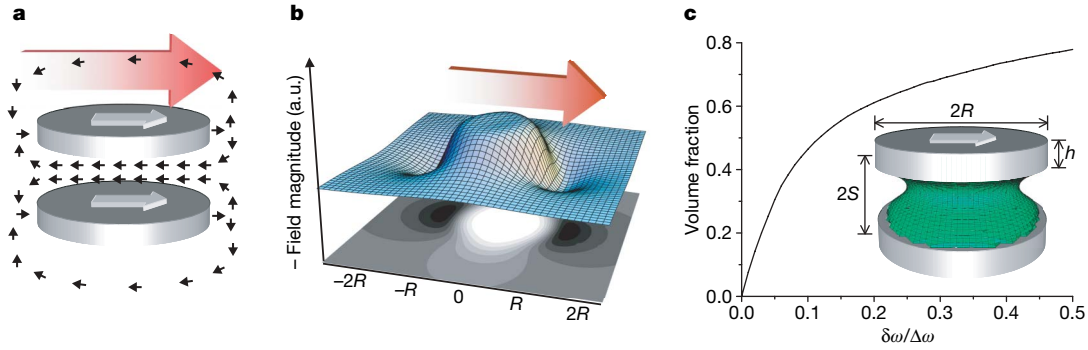

Figure 1 | Magnetic structure and field diagrams. a, Diagram of the field (black arrows) from two parallel disks magnetized to saturation by B_0 (red arrow). Non-magnetic spacer elements are omitted for clarity. **b**, Calculated (negative) field magnitude in the mid-plane through a typical magnetized disk set, contrasting its homogeneous nature between the disks with its rapid external decay. **c**, Calculated particle volume fraction that falls within a bandwidth, $\delta\omega$, about the particle's frequency shift, $\Delta\omega$. A sample numerical surface contour delineates the characteristic extent of this homogeneously shifted field region; all points inside the green contour shell have shifts within $\Delta\omega \pm \Delta\omega/50$.

the preparatory pulse train at the particle resonance allows spatial MRI of the transferred magnetization saturation, as shown in Fig. 5. By selectively blocking particle interiors, Fig. 5 also confirms that the signals arise specifically from water diffusing through the particles. Because the required time, τ_d, for self-diffusion to 'refresh' the internal water scales with R^2, the saturated magnetization falls only linearly with R, not with volume $\sim R^3$, as particle size is reduced. Without diffusion, the effective 'refresh' time would be limited by the longitudinal relaxation time, $T_1 \approx 2$–3 s. For water self-diffusivity, $D = 2.3 \times 10^{-9}\,m^2\,s^{-1}$, the distance diffused during this period, $(6DT_1)^{1/2} \approx 0.2$ mm, effectively sets the size below which open structures gain in sensitivity. This size is two orders of magnitude larger than typical micrometre-sized particles that might be used for cell labelling. Compared to structures that might have an enclosed internal volume of water, the gains in signal-to-noise ratio from diffusion through micrometre-sized open structures are therefore of order 10^4.

The double-disk structures afford a specific example of this magnetization exchange principle. Although we typically use first-principles Monte Carlo simulation (see Methods) to quantitatively predict exact diffusion-driven magnetization saturation levels, rough analytic approximation is also possible. Because of the high shifted-field homogeneity of the double-disk structures, we can suppress background signal while still saturating out about one-third of the volume between the disks via off-resonant excitation pulses with bandwidths just a few per cent of the particle's shift (Fig. 1c). For $h \ll 2S \approx R$, the magnetic moment of the water saturated in a single pulse is therefore $m_{pulse} \approx M_0 \pi R^3/3$, for M_0 the equilibrium B_0-aligned proton magnetization. Because not all the water exchanges between consecutive pulses, however, this per-pulse magnetic saturation falls with subsequent pulses. For an inter-pulse delay, $\tau_d = R^2/6D$, simulations show a resulting per-pulse average saturation of about $m_{pulse}/2$. The spatial distribution of any single pulse of this saturated magnetization at some later time, $t \gg \tau_d$, can be approximated by analogy to an instantaneous point-source diffusion problem, giving the local magnetization saturation $M_S(r,t) \approx (m_{pulse}/2)(4\pi Dt)^{-3/2}\exp(-r^2/4Dt)\exp(-t/T_1)$, where the final factor accounts for relaxation back into alignment with B_0, and r measures distance from the particle. Within a characteristic diffusion distance, $d \equiv (DT_1)^{1/2}$, a τ_d-spaced train of such pulses rapidly (order T_1) approaches the steady-state distribution, $M_S(r) \approx (M_0/4)(R/r)\exp(-r/d)$. Integrating over a (spherical) voxel of radius $R_v \gg R$, with $R_v \ll d$, gives the approximate fractional magnetization

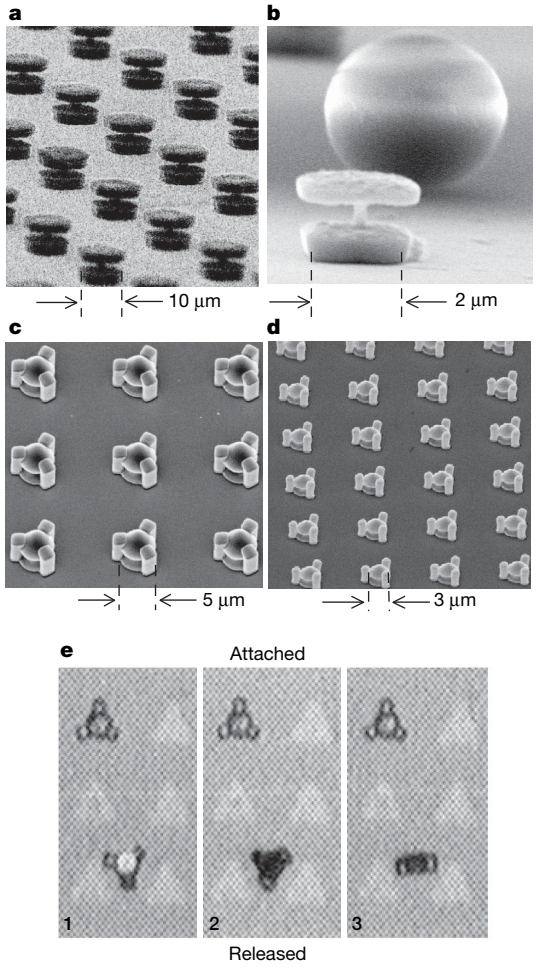

Figure 2 | Microfabricated magnetic structures. **a**, **b**, Scanning electron microscope (SEM) image of microfabricated double-disk magnetic structures with $R \approx 5$ μm (**a**) and $R \approx 1$ μm (**b**); the structures have non-magnetic internal supports. For relative size, a normal commercial 4.5 μm diameter MPIO (as commonly used for cell labelling/magnetic separation) is shown in the background in **b**. **c**, **d**, SEM image of externally supported double-disk structures with $R = 2.5$ μm (**c**) and R = 1.5 μm (**d**). In contrast to **a** and **b**, these particles demonstrate relatively thin magnetic layers, $h = 50$ nm, spaced $2S = 2$ μm (**c**) and 1 μm (**d**) apart. (The dome-like appearance of the top surfaces is due to a non-magnetic capping layer used during microfabrication.) These structures are robust, showing no discernible physical or magnetic change after month-long storage periods (both in and out of water). **e**, Optical micrograph contrasting a particle still attached to the substrate against an $R = 5$ μm particle released into water and automatically self-aligning with an applied magnetic field (of ~1 G) that is rotated from in-plane to out-of-plane in the sequence 1, 2, 3.

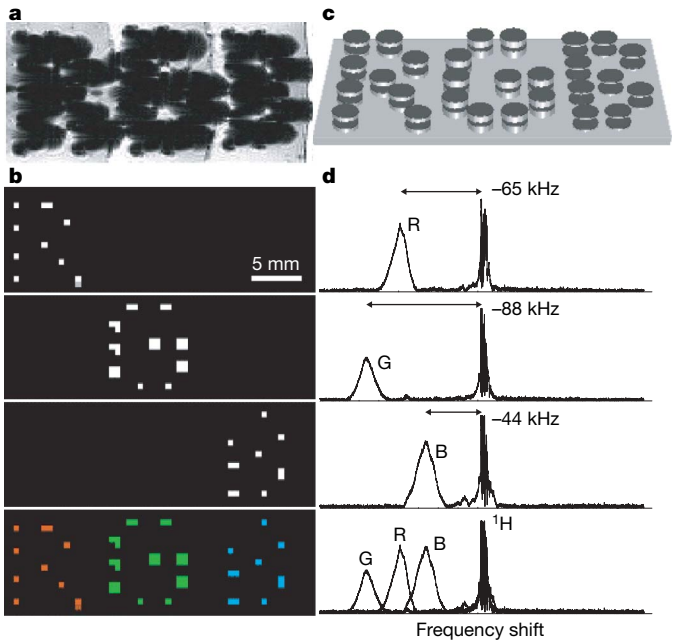

Figure 3 | Multi-spectral MRI. **a**–**d**, Chemical shift imaging of demonstration 1.25-mm-diameter particles magnetized by B_0. Particle frequency was varied by changing the thickness of electroplated nickel layers that formed the magnetizable disk pairs. As with normal SPIO detection, magnetic dephasing due to the particles' external fields enables the spatial imaging shown in the gradient-echo MRI (**a**). However, comparison between **a** and the chemical shift images (**b**) shows that the additional spectral information both differentiates between particle types and improves particle localization. The particles are shown schematically (not to scale) in **c**. With particle spectra (**d**, to the right of the corresponding chemical shift images in **b**) shifted well clear of the water proton line, different planes in the chemical shift imaging map isolate different particle types for unambiguous colour-coding with minimal background interference (**b**, bottom panel). (Although still visible in the gradient-echo image, the top corner particle of the letter 'B' was damaged, causing its shifted frequency peak to vanish.)

saturation of the water in the voxel immediately surrounding the particle as $M_S/M_0 \approx 0.3R/R_\gamma$. This linear rather than cubic scaling means, for example, that a sample $R = 2.5\,\mu m$ particle shown in Fig. 2c can saturate around 1–2% of a 50 μm radius voxel, even though its resonant field volume constitutes just 0.003% of that voxel. Such gains raise the possibility of simultaneous single microparticle imaging and spectral identification (as suggested in Fig. 5 legend) without the need for specialized microcoils[31]; indeed, all imaging described here was done with macroscopic surface and solenoidal coils up to several centimetres in diameter.

Comparison with traditional MRI agents

To compare the micro-engineered approach with traditional chemically synthesized agents, we turn from individual particle identification to detectable concentrations. Including continual longitudinal relaxation, the magnetic moment saturated out per particle pulsed over a period of $2T_1$ is $(m_{pulse}/2)(T_1/\tau_d)(1-e^{-2})$. Conservatively assuming at least 5% fractional saturation for reliable detection, required concentrations for micrometre-sized particles are therefore of order 10^{-14} M or, in elemental terms (assuming iron disks of aspect ratios similar to those of the particles in Fig. 2c), 0.01 mmol Fe l^{-1}. These concentrations are already below typical PARACEST concentrations used[7], an order of magnitude less than the clinical dosages of gadolinium relaxivity-based contrast agents in blood[5,32], and equal to those of SPIO agents[6]. However, as required concentrations scale with R^2, sub-micrometre structures that could be created using deep-ultraviolet or electron-beam lithography should substantially further reduce this concentration limit. Ultimately, the extent of the signal amplification that can be gained from this R^2 scaling is limited not by lithography, but by τ_d. By analogy with the 'slow-exchange' restriction[7] on chemical exchange processes, here diffusional exchange should not be so fast as to broaden the spectral peak by more than its shift. Fortunately, because large shifts can be generated, this exchange broadening becomes a limiting factor only below the 100 nm scale, at which point required metal concentrations would be in the nanomolar regime. Although this size scale may be regarded as a disadvantage over molecular-based agents, interest in MPIOs[19–21] indicates a growing range of applications for MRI contrast agents of similar, or even larger, size. Note, however, that while the 100 nm scale limits signal gained from further size reduction, it need not necessarily represent an absolute minimum structure size. Still smaller structures could be used by partially blocking access to the double-disk interior or by switching to an alternative less open structure to intentionally limit the effective exchange rate and keep τ_d within a desirable range. As sizes shrink further, the attendant shortening τ_d may also dictate that the preparatory RF pulse trains transform into quasi-continuous pulses; depending on the situation, such partial throttling of the water diffusion may also be desirable here.

Discussion

The faster imaging and increased safety margins that the structures' low concentration requirements imply are a consequence not only of faster allowable exchange rates, but also of the extended homogeneous field regions that can exchange many spins simultaneously, as

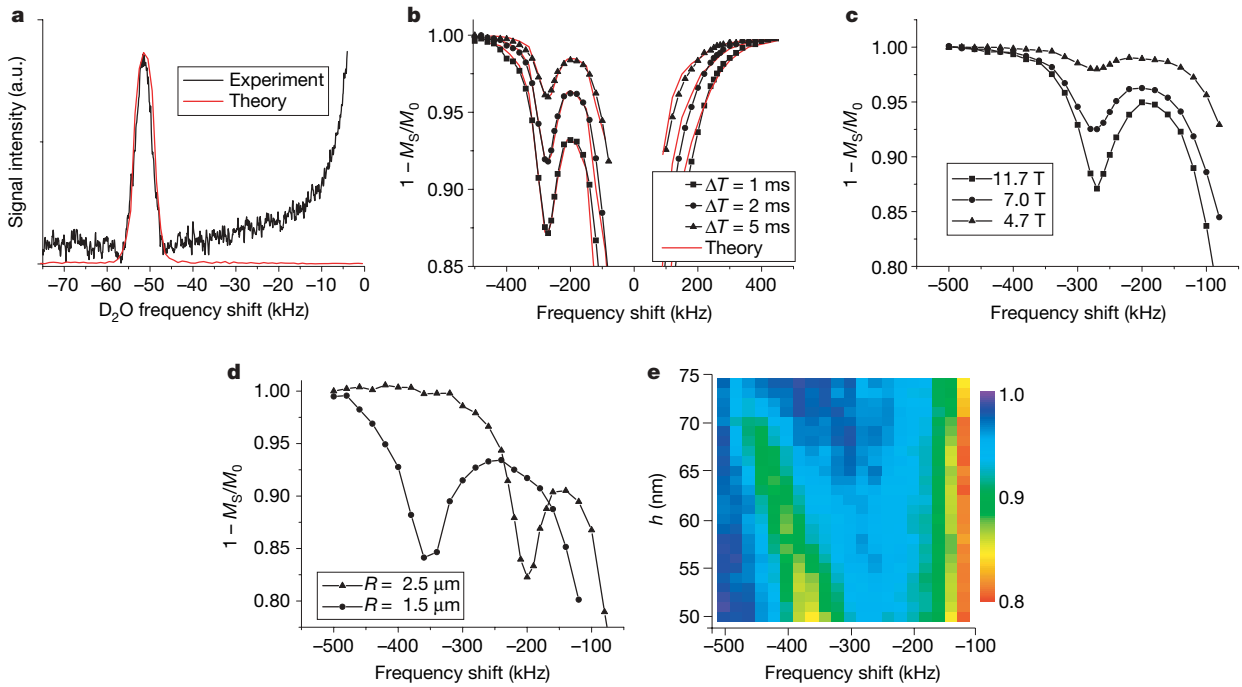

Figure 4 | Engineered spectral shifting. **a**, Fourier transformed spin-echo signal, showing direct imaging at 11.7 T of a spectrally shifted deuterium oxide peak from a set of $R = 12.5\,\mu m$ particles submerged in D_2O. Apart from overall signal magnitude, there are no free fitting parameters. **b**, $R = 2.5\,\mu m$ particle H_2O z-spectra taken at 7 T show increasing fractional saturation (M_S/M_0) with shortening delays, ΔT, between off-resonant $\pi/2$ pulses. Overlaid theory is derived from first-principles Monte Carlo simulation (see Methods) and contains no free fitting parameters. **c**, $R = 2.5\,\mu m$ particle H_2O z-spectra for $\Delta T = 2$ ms at three different field strengths, showing frequency shifting independent of B_0. **d**, H_2O z-spectra demonstrating different frequency shifts from structures with different values of R, but with fixed $h = 50$ nm and approximately constant $S/R \approx 0.3$–0.4. Because **c** and **d** assemble data from different MRI magnets and coils, comparative theory overlays are less meaningful, but data remain in agreement with theory. **e**, Continuous frequency-pulling engineered through continuously changing h (each row in the image shows the experimental H_2O z-spectrum for a different particle disk thickness, with the colour shading indicating the value of $1 - M_S/M_0$ at each point). For completeness, we show everywhere raw z-spectra of the shifted peaks atop the unshifted broadened water background; because the surrounding water broadening is approximately symmetric, however, this background can be eliminated by considering differences between corresponding positive- and negative-frequency saturations. All data are from first-generation test particle arrays with as yet still suboptimal geometries and ~10% interparticle frequency-shift variation due to cross-wafer manufacturing variation. Improved fabrication should reduce variation to below 1% and aid geometry optimization, substantially narrowing linewidths and increasing saturation levels.

opposed to the individual exchangeable proton sites of molecular complexes[7]. Micro-engineering also enables the use of biologically benign materials, allowing these field regions to be directly accessible and eliminating the efficiency-versus-toxicity trade-offs of agents based on chelated lanthanide ions[5,32]. Additionally, ferromagnetic or superparamagnetic materials ensure full saturation even for small B_0, enabling lower imaging fields while retaining large, field-independent shifts (Fig. 4c).

In principle, spectrally distinct, physiologically responsive indicators could also be formed by either encapsulating the particles, or filling their internal regions, to inhibit internal diffusion (Fig. 5) while leaving their external spatially trackable image-dephasings unaffected. If the material that blocks entry of water into the structures is chosen to be vulnerable to specific enzymatic attack, or to dissolution beyond a certain temperature or pH, subsequent water diffusion could effectively 'turn on' their spectral signals. Conversely, the spacer elements could be made from some dissolvable or reactive material to effectively modify or completely 'turn off' the spectral signals. Orientation-dependent sensors should also be possible by varying geometry to decrease magnetic self-alignment, yielding signals that appear or disappear depending on particle orientation. With spectral differentiation enabling multi-particle co-registration within the same voxel, a variety of multiplexed diagnostics can be envisaged. Additionally, their open structures and large shift ranges are well suited for flow and perfusion studies with multiple spin-labelled streams. Moreover, beyond MRI, their subcellular size may enable RFID-based microfluidics.

In conclusion, engineering local field environments over subcellular size-scales through tailored microstructures appears a promising avenue to a variety of new imaging and/or sensing mechanisms. Micrometre-sized structures can be microfabricated with a broad range of spectral coverage, and advanced lithographic techniques should enable substantial further decreases in the sizes of these structures, bringing them close to the sizes of nanoparticles at present in clinical use. Particularly encouraging are the design latitudes afforded by the high sensitivity of these micro-engineered agents, raising the possibility of a variety of additional microstructures that may similarly increase MRI functionality and impact.

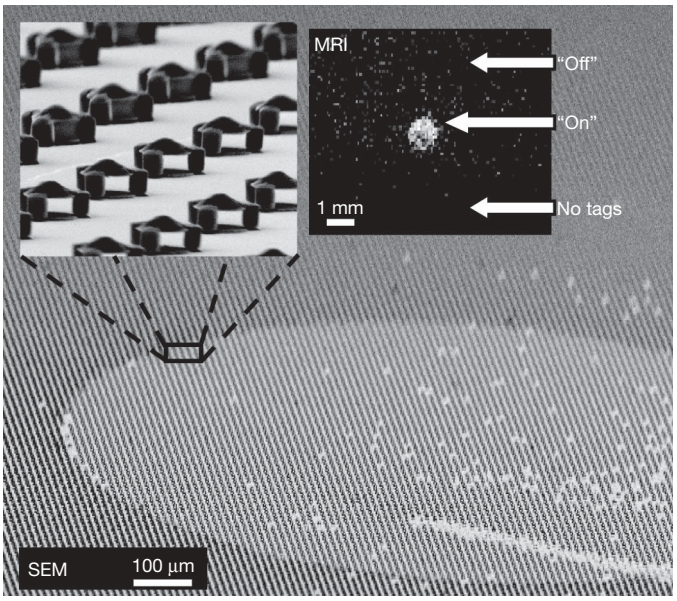

Figure 5 | Controlling diffusion to turn tags on or off. Main panel, high tilt-angle SEM image showing a square array of $R = 2.5$ μm particles. Except for a defined circular region, all particles have their interiors filled, blocking water diffusion. Top left inset, a higher magnification SEM image of the boundary between open and filled particles. Top right inset, the resulting background-subtracted chemical shift MRI showing transferred magnetization saturation from the particles' shifted resonance. Signal is visible from those particles that have water diffusing through their open interior region (labelled 'On') but not from those particles that have their interiors filled (labelled 'Off'). The bottom of the image shows a region that contains no particles (labelled 'No tags'), providing a null background signal comparison. A scratch (seen at the lower right corner) removed ~100 particles (about 10–20 per voxel). Its visibility in the magnetic resonance image suggests the potential for high-resolution imaging to spectrally distinguish individual such particles.

METHODS SUMMARY

Experimental set-up. Apart from the magnetic self-alignment experiments that involved freely floating particles in water, in order to enable more precise analysis, control experiments were performed on defined grids of test particles (13 mm × 13 mm square) attached to diced 15 mm × 15 mm Pyrex substrates on which the particles were originally microfabricated. Interparticle grid spacings (centre-to-centre) were typically 3 to 4 times the particle diameter, at which point numerical field calculations showed that any influence from the external fields of neighbouring particles had decayed to negligible levels. Individual Pyrex chips were sealed in custom-made holders filled with either water or deuterium oxide to a depth of at least 150 μm, sufficient to deeply submerge the particles and to continue well beyond the extent of any appreciable external particle field decays. Each of the water- or deuterium oxide-submerged samples were then individually placed next to, or inside, surface or solenoidal radio-frequency (RF) coils, respectively, for transmission/reception of the relevant NMR signals.

Numerical simulations. To help verify the physical understanding and analytical approximations presented, first-principles Monte Carlo simulations were also performed. These simulations modelled the effects of the applied RF field pulses and the (numerically calculated) fields of the magnetized double-disk microstructures on the local water, or deuterium oxide, nuclear spin evolution. Within the accuracy of our measurements we find good agreement with experiment (Fig. 4a, b), suggesting that the presented models capture the dominant physical processes involved.

Full Methods and any associated references are available in the online version of the paper at www.nature.com/nature.

Received 26 December 2007; accepted 21 April 2008.

1. Lauterbur, P. C. Image formation by induced local interactions: Examples employing nuclear magnetic resonance. *Nature* **242,** 190–191 (1973).
2. Mansfield, P. & Grannell, P. K. NMR 'diffraction' in solids? *J. Phys. C* **6,** L422–L426 (1973).
3. Callaghan, P. T. *Principles of Nuclear Magnetic Resonance Microscopy* (Oxford Univ. Press, New York, 1991).
4. Nelson, K. L. & Runge, V. M. Basic principles of MR contrast. *Top. Magn. Reson. Imag.* **7,** 124–136 (1995).
5. Runge, V. M. & Wells, J. W. Update: Safety, new applications, new MR agents. *Top. Magn. Reson. Imag.* **7,** 181–195 (1995).
6. Weissleder, R. *et al.* Ultrasmall superparamagnetic iron oxide: Characterization of a new class of contrast agents for MR imaging. *Radiology* **175,** 489–493 (1990).
7. Woods, M., Woessner, D. E. & Sherry, A. D. Paramagnetic lanthanide complexes as PARACEST agents for medical imaging. *Chem. Soc. Rev.* **35,** 500–511 (2006).
8. Lanza, G. M. *et al.* $^{1}H/^{19}F$ magnetic resonance molecular imaging with perfluorocarbon nanoparticles. *Curr. Top. Dev. Bio.* **70,** 57–76 (2005).
9. Mason, W. T. (ed.) *Fluorescent and Luminescent Probes for Biological Activity* (Academic, London, 1999).
10. Bruchez, M. Jr, Moronne, M., Gin, P., Weiss, S. & Alivisatos, A. P. Semiconductor nanocrystals as fluorescent biological labels. *Science* **281,** 2013–2016 (1998).
11. Chan, W. C. W. & Nie, S. Quantum dot bioconjugates for ultrasensitive nonisotopic detection. *Science* **281,** 2016–2018 (1998).
12. Alivisatos, P. The use of nanocrystals in biological detection. *Nature Biotechnol.* **22,** 47–52 (2004).
13. Elghanian, R., Storhoff, J. J., Mucic, R. C., Letsinger, R. L. & Mirkin, C. A. Selective colorimetric detection of polynucleotides based on the distance-dependent optical properties of gold nanoparticles. *Science* **277,** 1078–1081 (1997).
14. Haes, A. J. & Van Duyne, R. P. A nanoscale optical biosensor: Sensitivity and selectivity of an approach based on the localized surface plasmon resonance spectroscopy of triangular silver nanoparticles. *J. Am. Chem. Soc.* **124,** 10596–10604 (2002).
15. Nicewarner-Peña, S. R. *et al.* Submicrometer metallic barcodes. *Science* **294,** 137–141 (2001).
16. Dodd, S. J. *et al.* Detection of single mammalian cells by high-resolution magnetic resonance imaging. *Biophys. J.* **76,** 103–109 (1999).
17. Cunningham, C. H. *et al.* Positive contrast magnetic resonance imaging of cells labeled with magnetic nanoparticles. *Magn. Reson. Med.* **53,** 999–1005 (2005).

18. Bulte, J. W. M. *et al.* Magnetodendrimers allow endosomal magnetic labeling and *in vivo* tracking of stem cells. *Nature Biotechnol.* **19,** 1141–1147 (2001).
19. Hinds, K. A. *et al.* Highly efficient endosomal labeling of progenitor and stem cells with large magnetic particles allows magnetic resonance imaging of single cells. *Blood* **102,** 867–872 (2003).
20. Shapiro, E. M., Skrtic, S. & Koretsky, A. P. Sizing it up: Cellular MRI using micron-sized iron oxide particles. *Magn. Reson. Med.* **53,** 329–338 (2005).
21. Wu, Y. L. *et al.* In situ labeling of immune cells with iron oxide particles: An approach to detect organ rejection by cellular MRI. *Proc. Natl Acad. Sci. USA* **103,** 1852–1857 (2006).
22. Kotzar, G. *et al.* Evaluation of MEMS materials of construction for implantable medical devices. *Biomaterials* **23,** 2737–2750 (2002).
23. Voskerician, G. *et al.* Biocompatibility and biofouling of MEMS drug delivery devices. *Biomaterials* **24,** 1959–1967 (2003).
24. Chikazumi, S. *Physics of Ferromagnetism* (Oxford Univ. Press, New York, 1997).
25. Bozorth, R. M. *Ferromagnetism* (Van Nostrand, New York, 1951).
26. Sato, M., Wond, T. Z. & Allen, R. D. Rheological properties of living cytoplasm: Endoplasm of *Physarum* plasmodium. *J. Cell Biol.* **97,** 1089–1097 (1983).
27. Ashkin, A. & Dziedzic, J. M. Internal cell manipulation using infrared laser traps. *Proc. Natl Acad. Sci. USA* **86,** 7914–7918 (1989).
28. Henkelman, R. M., Stanisz, G. J. & Graham, S. J. Magnetization transfer in MRI: A review. *NMR Biomed.* **14,** 57–64 (2001).
29. Zurkiya, O. & Hu, X. Off-resonance saturation as a means of generating contrast with superparamagnetic nanoparticles. *Magn. Reson. Med.* **56,** 726–732 (2006).
30. Grad, J. & Bryant, R. G. Nuclear magnetic cross-relaxation spectroscopy. *J. Magn. Reson.* **90,** 1–8 (1990).
31. Olson, D. L., Peck, T. L., Webb, A. G., Magin, R. L. & Sweedler, J. V. High-resolution microcoil ^{1}H-NMR for mass-limited nanoliter-volume samples. *Science* **270,** 1967–1970 (1995).
32. Shellock, F. G. & Kanal, E. Safety of magnetic resonance imaging contrast agents. *J. Magn. Reson. Imag.* **10,** 477–484 (1999).

Acknowledgements We thank the Mouse Imaging Facility at the NIH for use of the 4.7T magnet, and A. Silva for use of the 7T magnet. This work was supported in part by the NINDS NIH Intramural Research Program. G.Z. also acknowledges support from a National Research Council fellowship award.

Author Information Reprints and permissions information is available at www.nature.com/reprints. Correspondence and requests for materials should be addressed to G. Z. (zabow@boulder.nist.gov).

METHODS

MRI experimental details. For the direct spectral detection experiment using water (spectra of Fig. 3), free induction decay (FID) signals following a spin-echo were acquired by sweeping through a range of frequencies covering the expected offsets produced by the particles. Shaped pulses with a gaussian profile were used to limit bandwidth spread into the bulk water peak (as compared to a hard pulse). Their bandwidths were, however, sufficient to cover the frequency profiles produced by the particles. Acquisitions for the spectra were 8,192 points in length, covering a bandwidth of 100 kHz. For the associated RGB image, three two-dimensional chemical shift images were acquired, covering the frequency ranges of the particle spectra. Images are integrations of the spectra over the different frequency ranges. In-plane resolution was 500×750 μm. Particle geometrical parameters were $R \approx 625$ μm, $2S \approx 500$ μm, and $h \approx 4$, 6 and 8 μm. Accidental impurities in the nickel disks of these structures led to a reduced $J_S \approx 0.4$ T. (All other structures had purer nickel with $J_S \approx 0.5$–0.6 T.)

For the direction detection experiment using D_2O (Fig. 4a), FIDs following a spin-echo were acquired using as large a bandwidth as our coil would allow, 50 kHz. Particle geometrical parameters were $R \approx 12.5$ μm, $2S \approx 10$ μm and $h \approx 0.5$ μm.

For the indirect detection experiments (Fig. 4b–e), the pulse sequence consisted of a series of off-resonance pulses (gaussian shape, 100 μs in length) for a period of a few T_1s, preceding an on-resonance 90° pulse for collection of an FID. Each point in the z-spectra represents the integral of this FID for a different off-resonance frequency of the preparatory pulse train. The gap between each pulse in the preparatory pulse trains was varied between 1 ms and 5 ms. For experiments at different field strengths (4.7, 7, 11.7 T), differing B_1 profiles from the different coils used may have led to some variations in the results. Particle geometrical parameters were $R \approx 2.5$ μm, $2S \approx 2$ μm and $h \approx 65$ nm for Fig. 4b, c; $R \approx 2.5$ μm, $2S \approx 2$ μm and $h \approx 50$ nm, and $R \approx 1.5$ μm, $2S \approx 1$ μm and $h \approx 50$ nm for Fig. 4d.

To demonstrate the spatial imaging using the indirect detection (Fig. 5), chemical shift images were acquired after a series of pulses at the predetermined offset frequency (in this case −330 kHz). A baseline image without the preparatory sequence was used to provide a subtraction image. The in-plane image resolution was 100×100 μm, with the thickness being determined by the 150 μm water depth. To speed up the imaging, the repetition time T_R was set to 500 ms, with the preparatory sequence being run continuously between each T_R. Particle geometrical parameters were $R \approx 2.5$ μm, $2S \approx 2$ μm and $h \approx 80$ nm.

It should be noted that all of the geometrical particle parameters listed represent approximate values only. Variation in particle parameters was in general dominated by slight variations in the exact purity of the nickel (and hence its precise magnetic saturation value) and by variations in the thickness of the nickel disk layers of about 10% throughout.

MRI numerical simulations. Simulations of the MRI experiments, results of which are seen in the theoretical curve fits to the data of Fig. 4a (direct spectral imaging) and Fig. 4b (indirect diffusional exchange based imaging), were derived from full first-principles Monte Carlo simulations purposely coded for analysing the double-disk structure experiments. To ensure accurate results, the Monte Carlo simulations simultaneously tracked the position, orientation and phase of upwards of several million simulated nuclear spins (with discrete time-steps down to a microsecond). These spins were modelled simultaneously randomly diffusing through a three-dimensional water volume (that matched the dimensions of the chip sample holder) surrounding a two-dimensional grid of double-disk structures that corresponded to the test chip layouts. Cyclic boundary conditions were used to reduce the number of double-disk structures that needed to be simulated. Larmor frequencies at each spatial location in this volume (used to compute the total accumulated phase of each spin over its random walk) were calculated based on numerically integrated calculations of the fields from the array of magnetized double-disk structures. 90° off- and on-resonance pulses (and for the direct detection, also 180° spin-echo pulses) were simulated via reorientation of only those spins that fell within the simulated resonant bandwidth of the applied pulses, as determined by the local Larmor frequency shifts at the location of each spin. Because self-diffusion distances over periods of order 100 μs (the typical pulse durations) can be appreciable at the micrometre scale, care was taken to simulate diffusion not just between applied RF pulses, but also during each RF pulse. Continual T_1-longitudinal relaxation was accounted for by reorientation of a set percentage of randomly chosen spins back into alignment with B_0 during each integration time-step. Signal acquisition was simulated based on the (time-varying) integrated field of all those spins within the readout bandwidth over the duration of the final simulated FID or spin-echo acquisition; since this integrated field included all magnetic field vector information (from orientation and phase of each spin), coherence/dephasing information was retained. Such coherence information affects the direct imaging spin-echo spectra, but, apart from loss of transverse coherence between RF 90° pulses, it does not affect the indirect diffusional exchange experiments. For the direct spectral imaging, the simulated acquired spin-echo signals were then numerically Fourier-transformed to give the final spectra (such as that shown in Fig. 4a); for the indirect diffusion-based imaging, the total percentage of spins saturated out, or essentially the integrated area under the simulated FID, gives the value of any point in the z-spectra shown in Fig. 4b (that is, the simulation is rerun for each point in the z-spectra instead of the single simulation run required for any direct imaging spectrum).